Scripta Materialia 274 (2026) 117135

Contents lists available at ScienceDirect

Scripta Materialia

journal homepage: www.journals.elsevier.com/scripta-materialia

Can the grain boundary stiffness driving force explain observed grain boundary migration rates in polycrystals?

Zipeng Xu [a], Fadi Abdeljawad [b,c], Gregory S. Rohrer [a,*,#]

[a] Department of Materials Science and Engineering, Carnegie Mellon University, Pittsburgh, PA 15213, USA
[b] Department of Materials Science and Engineering, Lehigh University, Bethlehem, PA 18015, USA
[c] Department of Materials Science and Engineering, Northwestern University, Evanston, IL 60208, USA

ARTICLE INFO

Keywords:
Grain boundary
Grain growth
Grain boundary stiffness
Grain boundary migration

ABSTRACT

The anisotropic grain boundary stiffness driving force is compared to observed grain boundary migration rates in Ni polycrystals for five grain boundary disorientations. Although the stiffness driving force is better correlated to observed migration rates than the curvature driving force, neither correlation is strong. These findings might be the result of a limitation in the theory for grain boundary migration, which treats grain boundaries as independent microstructural entities and ignores the constraints imposed by their connections to other boundaries at triple lines.

In three-dimensions, a grain boundary has five independent parameters, three for the disorientation and two for the orientation of the normal to the grain boundary plane ($\hat{\mathbf{n}}$) [1]. Because the grain boundary energy depends on the grain boundary normal, the driving force for grain boundary migration (F_S) depends on the grain boundary inclination and curvature and can be expressed as [2–5]:

$$F_S = \Gamma(\hat{\mathbf{n}}) : K \tag{1}$$

where $\Gamma(\hat{\mathbf{n}})$ is the second-rank interfacial stiffness tensor, K is the second-rank curvature tensor, and : is the double dot product, $\Gamma(\hat{\mathbf{n}}) : K = \text{trace}\left(\Gamma(\hat{\mathbf{n}})K^T\right)$. Throughout this letter we will refer to F_S as the stiffness driving force. Assuming the principal directions of the interfacial stiffness tensor and curvature tensor are aligned, then at a point on the boundary, this expression reduces to:

$$F_S = \left(\gamma(\hat{\mathbf{n}}) + \frac{\partial^2\gamma(\hat{\mathbf{n}})}{\partial\theta^2}\right)\kappa_1 + \left(\gamma(\hat{\mathbf{n}}) + \frac{\partial^2\gamma(\hat{\mathbf{n}})}{\partial\phi^2}\right)\kappa_2 \tag{2}$$

where γ is the grain boundary energy, κ_1 and κ_2 are principal curvatures (the eigenvalues of the curvature tensor), and θ and ϕ are polar and azimuth angles, respectively, for the interface normal direction in spherical coordinates ($\hat{\mathbf{n}}(\theta,\phi)$) [6].

In practice, Eq. (1) is typically simplified to the scalar equation [7]:

$$F_C = \gamma\kappa \tag{3}$$

where κ is the mean curvature. The quantity F_C will be referred to as the conventional driving force. For the case of bicrystals, Eq. (3) has proven useful [8]. However, with the availability of 3D X-ray microscopy, Eq. (3) has been subjected to experimental tests in polycrystals and the results suggest it is not operative [9–12]; these findings have been supported by simulations [13–16].

This leads to the question, can the stiffness driving force better account for the observed migration rates of grain boundaries in polycrystals than the conventional driving force? Eq. (1) has been neglected in the analysis of experimental results because of its complexity. One factor that complicates the use of Eq. (1) is that $\Gamma(\hat{\mathbf{n}})$ differs for each possible misorientation and the function $\gamma(\hat{\mathbf{n}})$ in not generally known. Even though it is possible to compute the stiffness of grain boundaries by simulation [17–21], simulated stiffnesses for all possible boundaries at a fixed misorientation are not yet available. A second factor is that Eq. (1) is valid only for non-singular grain boundaries; for singular grain boundaries the driving force must be calculated by considering the change in the energies of the neighboring boundaries attached to the triple lines at the edges of the singular boundary [6,22,23]. The first of these difficulties has recently been overcome – twice differentiable functions for $\gamma(\hat{\mathbf{n}})$ have been defined at five misorientations for Ni [2,5]. Using these functions, one can compute the stiffness values necessary to

* Corresponding author.
E-mail address: gr20@andrew.cmu.edu (G.S. Rohrer).
"Gregory Rohrer was an Editor of the journal during the review period of the article. To avoid a conflict of interest, Gregory Rohrer was blinded to the record and another editor processed this manuscript."

https://doi.org/10.1016/j.scriptamat.2025.117135
Received 8 September 2025; Received in revised form 9 November 2025; Accepted 4 December 2025
Available online 11 December 2025

test Eq. (1). In this letter, we compare the observed grain boundary migration velocities in Ni [9] to the stiffness driving force defined by Eq. (1). We show that the stiffness driving force has much greater variations than the conventional driving force. Furthermore, while the stiffness driving force shows a correlation to the velocities of 60°/[111] tilt boundaries, there is little correlation throughout the remainder of the data.

The experimental velocities were derived from 3D Ni microstructures measured before and after five 30 min anneals at 800 °C by high-energy diffraction microscopy (HEDM). During the annealing, the average grain size increased from 19 μm to 23 μm, which translates to an increase from 1149 to 2055 voxels per average grain. Details of the sample preparation procedures, the experiment, and previous analyses of these publicly accessible data [24] can be found in prior publications [25,26]. Briefly, the microstructures were reconstructed using Dream.3D [27], and grain boundaries were approximated by triangular meshes using surface meshing [27] and Laplacian smoothing [28]. The complete data pipeline is available within the Dream.3D files in the archive [24] and the details of the smoothing procedure are described in the §S1 in the supplemental materials. Grain boundary velocity was calculated using the voxel exchange method that was described in previous work [9,11]. Grain boundary curvature was computed using the cubic-order algorithm [29]. From those calculations, the principal curvatures (κ_1, κ_2) and their corresponding principal directions ($\mathbf{K}_1$, $\mathbf{K}_2$) were extracted, along with the five grain boundary parameters for each triangular mesh element. Grain boundaries with the target misorientation were extracted (using $a \pm 5°$ acceptance range) from the entire data set using 3D_dist_graph [30].

To compute the driving force based on the stiffness and curvature tensors, it is essential to express both in a common reference frame. The interfacial stiffness tensor is defined in a spherical coordinate system where the poles are aligned to defined crystallographic directions while the curvature tensor is computed in the sample frame based on reconstructed microstructure data. Therefore, a two-step transformation is applied: (1) the principal curvature directions and surface normal are transformed to the crystal reference frame and (2) the curvature tensor is transformed into the same spherical coordinate system used by the stiffness tensor (which is not the same for each misorientation and defined in [2,5]). These transformations, detailed in sections S2 and S3 of the supplemental materials, are illustrated schematically in Fig. 1.

There are two numerical issues that affect the interpretation of the results. The first is that some of the computed stiffness values are negative. This happens for orientations that are not part of the equilibrium bicrystal shape [2]. Grain boundaries with these "missing orientations" will form faceted structures. The facets that make up the boundary will have the orientations of grain boundaries that are part of the equilibrium shape and closest to the missing orientation. The stiffness driving force does not apply to such orientations because the grain boundaries are comprised at least in part of singular boundaries and the driving force for these boundaries is determined instead by the adjacent connected boundaries [31]. The second issue is that the parameterization of the orientation by spherical angles leads to a numerical divergence near the z-axis of the stiffness reference frame. This is because the stiffness calculation includes terms of $\sin\theta$ and $\sin^2\theta$ in the denominator (see Eq. S3) and as the polar angle θ becomes very small, these terms diverge to infinity. For example, for the 60°/[111] grain boundary, the z-axis is positioned along the [111] crystal direction which leads to an undefined stiffness at this orientation.

The grain boundary properties of the 60°/[111] (Σ3) grain boundaries are presented in Fig. 2. The red triangle in Fig. 2(d) marks the orientation of the coherent twin boundary, which is the minimum in the distribution of grain boundary velocity (Fig. 2a). The principal stiffness distributions are shown in Fig. S2, where orientations with negative principal stiffness are colored black. The stiffness driving force ($\mathbf{\Gamma}(\hat{\mathbf{n}}) : \mathbf{K}$) and the conventional driving force ($\gamma\kappa$) are illustrated in Fig. 2 (b) and (c), respectively. As mentioned above, the plane normal vector $\hat{\mathbf{n}} = (111)$ is aligned along the Z-axis for this grain boundary, so the results in the white area do not accurately reflect the driving force and should be disregarded.

Considering the orientations with negative stiffness and the orientations near [111] that must all be excluded, only the driving forces with orientations near the zone of tilt grain boundaries (those perpendicular to [111]) can be compared to the velocity. This comparison is illustrated in Fig. 3 for the stiffness driving force and for the conventional driving force. For each data point, the average values of velocity and driving forces were computed by considering all meshed triangles whose plane normals deviate by <7° from the target normal vector. Note that while data was extracted along the entire tilt axis on the projection shown in Fig. 2d, from $(\bar{1}10)$ to $(1\bar{1}0)$, only the segment of data for $\pi/8 < \omega < \pi/2$, where ω is the angle from $[\bar{1}10]$, is in a unique fundamental zone; the data outside this range are indistinguishable because of bicrystal symmetry. The stiffness driving force clearly exhibits a positive correlation with grain boundary velocity (Fig. 3(a)). On the other hand, the conventional driving force shows an inverse correlation with velocity (Fig. 3 (b)). It should also be noted that the stiffness driving force varies with orientation much more than the conventional driving force (see Fig. 3c), indicating that the conventional driving force is a poor approximation for these grain boundaries.

It is noteworthy that the stiffness driving force maximizes at orientations where the conventional driving force is a minimum. This is because of the shape of the grain boundary energy function. To illustrate this, consider the zone of tilt boundaries (the white dashed line in Fig. 2 or the abscissa in Fig. 3), the grain boundary energy function for 60°/[111] has a local maximum energy at the $(\bar{1}01)$ orientation and a local minimum energy at the $(\bar{1}\bar{1}2)$ orientation [2]. Therefore, the conventional driving force is greater at $(\bar{1}01)$ than at $(\bar{1}\bar{1}2)$. However, the

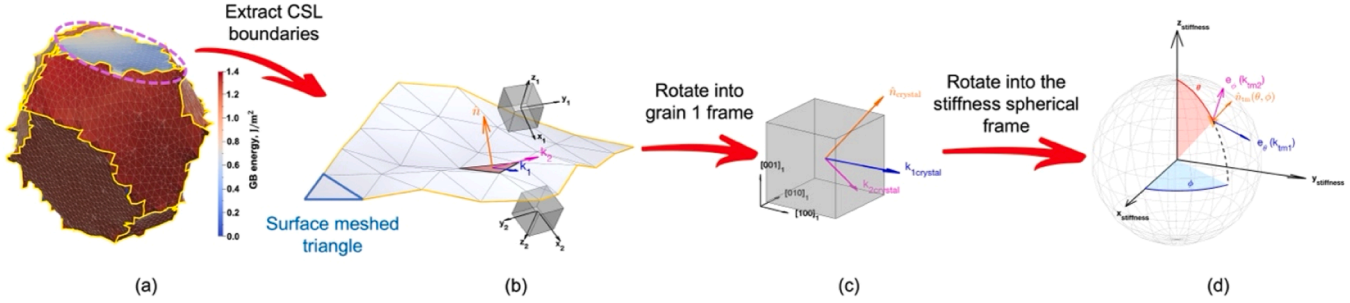

Fig. 1. The schematic illustration of the transformation that takes the normal vector ($\hat{\boldsymbol{n}}$) and principal directions ($\boldsymbol{K}_1$, $\boldsymbol{K}_2$) of the curvature tensor from the sample reference frame to stiffness-defined spherical coordinates. (a) A grain in the Ni polycrystals that was surface meshed by triangles, the yellow lines represent each grain boundary's outline (triple junctions), and grain boundaries are colored by their energies. (b) An extracted boundary with one of the target misorientations and the curvature reference frame of one triangular mesh on this boundary. (c) The vectors in the sample frame are transformed to the crystal frame of grain 1. (d) The vectors in the crystal reference frame are transformed to the stiffness reference frame and parameterized by spherical coordinates.

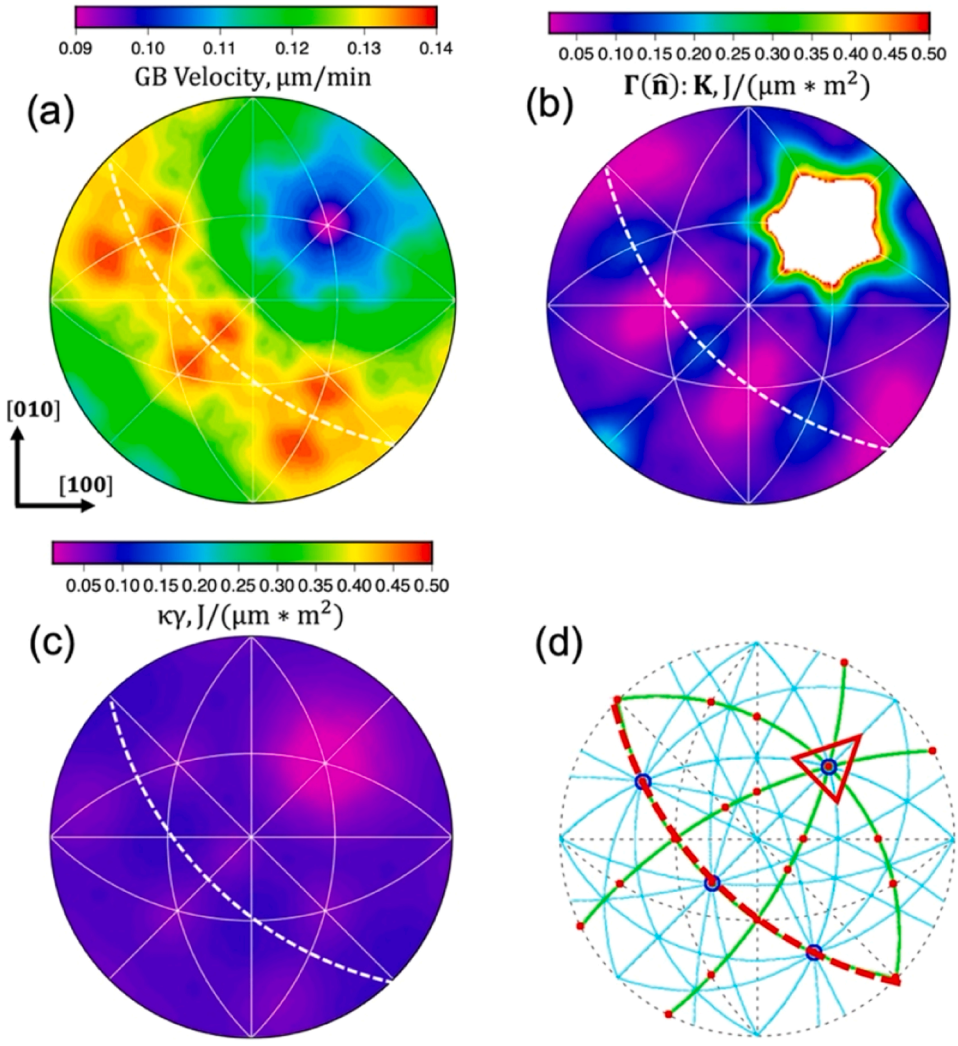

Fig. 2. Stereographic projections along [001] showing grain boundary property distributions for 12,085 60°/[111] grain boundaries comprised of 1580,821 individual mesh triangles. (a) Measured grain boundary velocity distribution. (b) Stiffness driving force distribution $\boldsymbol{\Gamma}(\hat{\boldsymbol{n}}) : \boldsymbol{K}$. The white region near [111] is excluded where $\boldsymbol{\Gamma}(\hat{\boldsymbol{n}}) : \boldsymbol{K} > 0.5$. (c) Conventional driving force distribution $\boldsymbol{\gamma\kappa}$. (d) Reference stereographic projection generated using GBTool box [32]. The red triangle denotes the coherent twin grain boundary orientation, while dashed lines represent tilt boundary orientations.

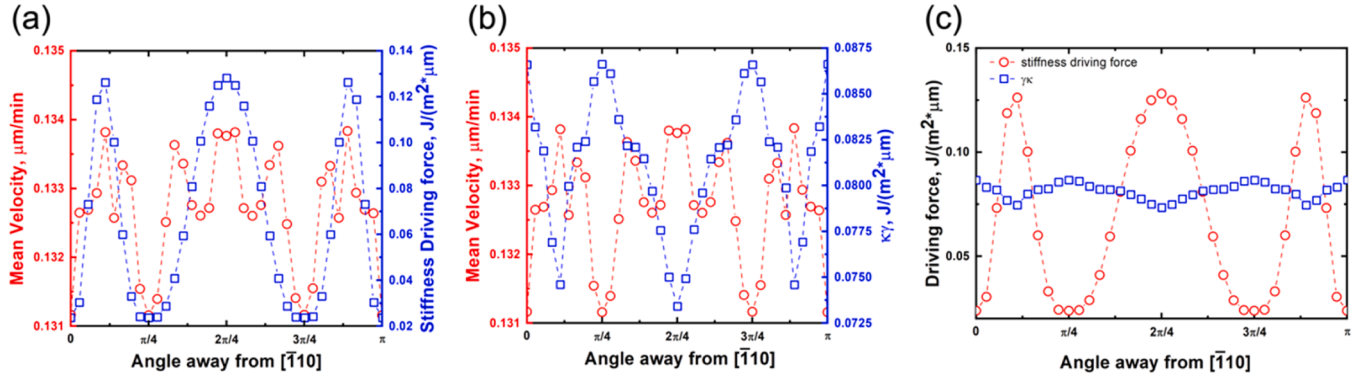

Fig. 3. Correlation between grain boundary velocity and driving forces as a function of angular deviation from $(\bar{1}10)$ for tilt boundaries with a 60°/[111] misorientation. Data points represent averaged values computed from all mesh triangles with plane normal deviating <7° from the target orientation vector. (a) Grain boundary velocity versus stiffness driving force $\boldsymbol{\Gamma}(\hat{\boldsymbol{n}}) : \boldsymbol{K}$. (b) grain boundary velocity versus conventional driving force $\boldsymbol{\gamma\kappa}$. (c) Comparison of the stiffness driving force $\boldsymbol{\Gamma}(\hat{\boldsymbol{n}}) : \boldsymbol{K}$ and conventional driving force $\boldsymbol{\gamma\kappa}$.

second derivative in the stiffness reverses this trend. As a simple example, take the $(\bar{1}01)$ orientation as the origin ($\phi = 0$) and assume the energy (γ) varies in one dimension (along the zone of tilt boundaries) as $\gamma = \cos\phi$. In this case, γ reaches a maximum at $\phi = 0$, but because $\partial^2\gamma/\partial\phi^2 = -\cos\phi$, the second derivative reaches a minimum at $\phi = 0$. For the actual grain boundary energy function, $\partial^2\gamma/\partial\phi^2 > \gamma$, so the second derivative dominates the stiffness. Therefore, it is the shape of the grain boundary energy function that causes the stiffness driving force to trend in the opposite way as the conventional driving force.

Grain boundary energy functions are also available for grain boundaries with misorientations of 37°/[100] (Σ5), 38°/[111] (Σ 7), 39°/[110] (Σ9), and 50°/[110] (Σ11) [5]. While boundaries with the 60°/[111] misorientation exhibit large regions of negative principal stiffness (Fig. S2), the principal stiffness distributions of these other boundaries predominantly display positive values (see Fig. S3). This characteristic enables the analysis of grain boundary velocity-stiffness driving force correlations across a broader range of plane normal directions for each boundary type. For this comparison, a hemisphere with 3096 discrete boundary plane orientations was sampled. For each of these misorientations, the stiffness driving force and boundary velocity were computed, excluding those positioned within 25° of the corresponding crystallographic Z-axis to avoid numerical instabilities (at smaller angles, $1/\sin^2\theta > 5$ and increases sharply). Because grain exchange symmetry reverses the sign of the stiffness, all other values were taken to be positive definite.

The results for the 39°/[110] and 50°/[110] grain boundaries are illustrated in Fig. 4, where each data point represents a unique boundary plane normal orientation, colored based on its relative area fraction within the total grain boundary population. The measured grain boundary velocities are only weakly correlated to the driving force, with $R^2 = 0.37$ and 0.43 for 39°/[110] and 50°/[110], respectively. The results for the 37°/[100] and 38°/[111] grain boundaries are shown in Fig. S4. For these boundaries, the velocity is uncorrelated to the driving force. However, the relative areas of these boundaries were near 1 MRD, indicating that they do not make up a large fraction of the data. The measured velocities are also compared to the conventional driving force in Fig. S5. With the exception of the 39°/[110] boundaries, which show a weak positive correlation ($R^2 = 0.39$), the other boundaries are not correlated to the conventional driving forces.

Throughout these comparisons, we have assumed the mobility term is constant, even though it is known to vary with grain boundary character [33]. For four of the misorientations, we can compare the mobilities determined by simulations with effective mobilities we estimate by dividing the observed velocity by the stiffness driving force. The results, illustrated in Figs. S6 and S7, do not alter the conclusions about the correlations. As illustrated in Fig. S6, the effective mobility and the computed mobility for the 60°/[111] tilt boundaries [2,33] are well correlated, similar to the stiffness and velocity. However, for the 37°/[100], 38°/[111], and 39°/[110] boundaries, illustrated in Fig. S7, there is no obvious correlation between the effective mobility and the computed mobilities.

When considering the results at all five boundaries, we conclude that while the stiffness driving force is better correlated to the observed velocity than the conventional driving force, neither driving force is a reliable predictor of the velocity. While a correlation was found for the 60°/[111] tilt boundaries, one cannot draw conclusions from only a subset of the data. It is interesting that the correlation is best for the most commonly observed grain boundaries. One might suggest that the comparison at other misorientations is limited by an insufficient number of observations. While this possibility cannot be ruled out, we note that the five boundaries sampled here make up 17.6 % of the 105,576 observed grain boundaries.

Another possibility is that the experimental time step is too coarse so that as boundaries migrate from the initial position, they change shape and the driving force therefore also changes; such changes could only be captured using smaller time intervals. Unfortunately, it is not possible to test this idea because we lack the spatial resolution to resolve smaller displacements. Another possible reason for the difference is that the assumptions in the derivation of the stiffness driving force are not well matched to the experiment. The derivation assumes that the grain boundaries can move without additional constraints. Although it has not been reported, one might assume that the migration of an isolated boundary in a bicrystal would be governed by the stiffness. In a polycrystal, on the other hand, all of the grain boundaries are connected. Because of this, it is impossible for any boundary to move without others moving and changing area at the same time, and this adds constraints to the motion. Additional constraints might arise from the necessity of annihilating grain boundary disconnections at the triple lines where the boundaries meet [34,35]. If the driving force is unable to overcome the constraints, then the motion will appear to be independent of the driving force, as described here.

To illustrate the motion of a single boundary and its lack of correlation with the stiffness, the initial position of a boundary (Fig. 5a) and the final position (Fig. 5b) are illustrated in Fig. 5. In both states, the boundary is discretized into triangular elements and they are colored by the stiffness driving force. We note that there are some outliers with very high stiffness found at the triple junctions, but we will ignore these in

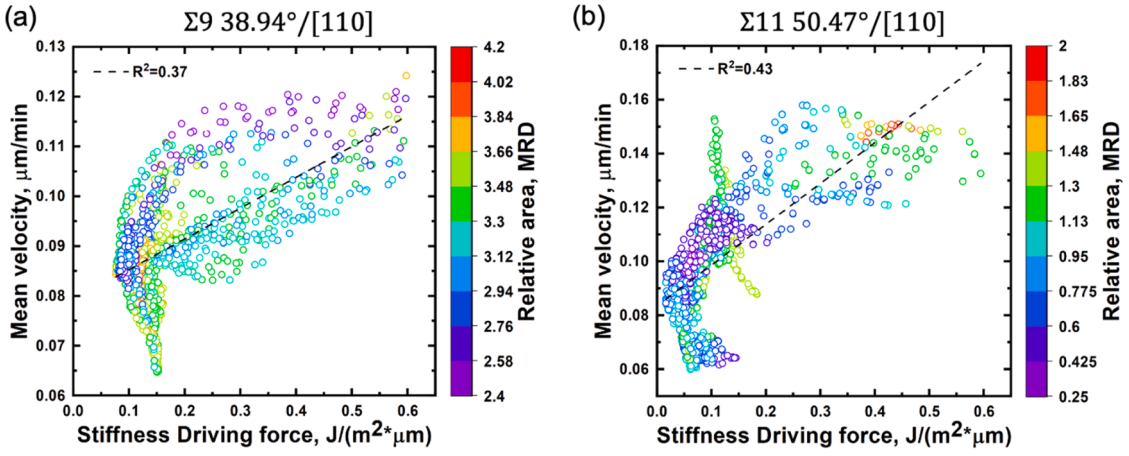

Fig. 4. Correlation between grain boundary velocity and the stiffness driving force for 39°/[110] and 50°/[110] grain boundaries. Each data point represents a distinct grain boundary plane normal orientation and is colored by the corresponding relative area fraction within the total grain boundary population (MRD scale). (a) Data from 4847 39°/[110] grain boundaries comprised of 837,206 mesh triangles. (d) Data from 811 50°/[110] grain boundaries comprised of 215,653 mesh triangles. Correlation coefficients (R^2) and fitted trend lines are indicated for each boundary type.

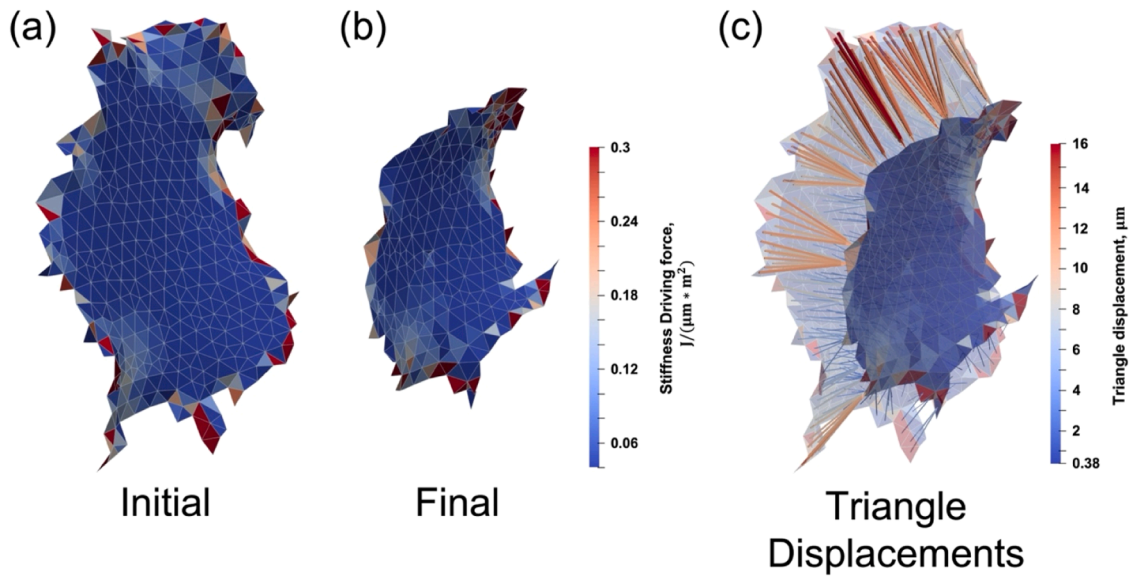

Fig. 5. Grain boundary evolution and qualitative meshed triangle trajectories during boundary migration. Meshed triangles are colored based on the corresponding stiffness driving force and arrows represent the displacement magnitude. (a) Initial state; (b) final state; (c) triangle displacement trajectories.

our analysis. Tracking individual triangular elements from the initial to the final position is not possible, as they change location, area, and total number. As a result, a simple mapping from initial triangles to final triangles does not exist. Therefore, we employed the shortest distance tracking method (see section S5 of the supplemental information for details) to qualitatively assess meshed triangle displacement trajectories across different states. Displacement vectors, colored by their magnitudes, are illustrated in Fig. 5(c). It is obvious in the figure that triangles with similar driving forces at different boundary regions do not show similar displacements (see also Fig. S8). For example, the triangles in the upper right part of the figure moved the farthest, but did not have driving forces significantly different from those on other parts of the boundary, such as the patch in the lower left of Fig. 5(a).

The illustration in Fig. 5, showing that parts of the boundary with similar driving force move very different distances, suggests that other driving forces are important in determining boundary motion. The patches of boundary migrating the greatest distance are near the periphery of the grain, suggesting the influence of the attached boundaries. It has been suggested that energy differences between boundaries that meet at junctions can provide an additional driving force for growth by the grain boundary replacement mechanism [36]. It has also been demonstrated by simulation that the stored elastic energy driving force can disrupt the expected relationship between curvature and velocity [16]. Under these circumstances, it is not surprising that the classical single-boundary migration equation fails to predict migration behavior, even when incorporating energy anisotropy effects through the stiffness driving force.

In summary, using available functions for the grain boundary energy of Ni, we evaluated correlations between the stiffness driving force and boundary migration velocity. Although the stiffness driving force is better correlated to the migration velocity than the conventional driving force, the evidence does not support the assertion that this driving force can be used to predict the migration of grain boundaries in a polycrystalline network. A potential explanation for these weak correlations lies in the inherent limitation of classical migration equations, which neglect network effects and consider only isolated boundary behavior. These findings suggest that developing improved grain boundary migration models will require incorporating the influence of interconnected boundary networks on individual grain boundary behavior, instead of treating each boundary as an isolated object.

CRediT authorship contribution statement

Zipeng Xu: Writing – original draft, Software, Investigation. **Fadi Abdeljawad:** Writing – review & editing, Methodology. **Gregory S. Rohrer:** Writing – review & editing, Methodology, Conceptualization.

Declaration of competing interest

The author Gregory S. Rohrer is Coordinating Editor for Scripta Materialia and was not involved in the editorial review or the decision to publish this article.

Acknowledgments

This work was supported by the National Science Foundation under DMREF Grant No 2118945.

Supplementary materials

Supplementary material associated with this article can be found, in the online version, at doi:10.1016/j.scriptamat.2025.117135.

References

[1] C. Goux, Structure of joined grains - crystallographic consideration and methods of structure estimation, Can. Metall. Quart. 13 (1974) 9–31, https://doi.org/10.1179/cmq.1974.13.1.9.
[2] F. Abdeljawad, S.M. Foiles, A.P. Moore, A.R. Hinkle, C.M. Barr, N.M. Heckman, K. Hattar, B.L. Boyce, The role of the interface stiffness tensor on grain boundary dynamics, Acta Mater. 158 (2018) 440–453, https://doi.org/10.1016/j.actamat.2018.06.025.
[3] D.X. Du, H. Zhang, D.J. Srolovitz, Properties and determination of the interface stiffness, Acta Mater. 55 (2007) 467–471, https://doi.org/10.1016/j.actamat.2006.08.038.
[4] J. Han, D.J. Srolovitz, M. Salvalaglio, Disconnection-mediated migration of interfaces in microstructures: I. continuum model, Acta Mater. 227 (2022) 117178, https://doi.org/10.1016/j.actamat.2021.117178.
[5] R.D. Moore, T. Beecroft, G.S. Rohrer, C.M. Barr, E.R. Homer, K. Hattar, B.L. Boyce, F. Abdeljawad, The grain boundary stiffness and its impact on equilibrium shapes and boundary migration: analysis of the Sigma 5, 7, 9, and 11 boundaries in Ni, Acta Mater. 218 (2021) 117220, https://doi.org/10.1016/j.actamat.2021.117220.
[6] C. Herring, Surface tension as a motivation for sintering, in: W.E. Kingston (Ed.), The Physics of Powder Metallurgy, McGraw-Hill, New York, 1951, pp. 143–179, https://doi.org/10.1007/978-3-642-59938-5_2.
[7] W.W. Mullins, 2-Dimensional motion of idealized grain boundaries, J. Appl. Phys. 27 (1956) 900–904, https://doi.org/10.1063/1.1722511.

[8] G. Gottstein, L.S. Shvindlerman, On the true dependence of grain-boundary migration rate on driving force, Scripta Metall. Mater. 27 (1992) 1521–1526, https://doi.org/10.1016/0956-716x(92)90138-5.
[9] A. Bhattacharya, Y.F. Shen, C.M. Hefferan, S.F. Li, J. Lind, R.M. Suter, C.E. Krill, G. S. Rohrer, Grain boundary velocity and curvature are not correlated in Ni polycrystals, Science (1979) 374 (2021) 189–193, https://doi.org/10.1126/science.abj3210.
[10] V. Muralikrishnan, H. Liu, L. Yang, B. Conry, C.J. Marvel, M.P. Harmer, G. S. Rohrer, M.R. Tonks, R.M. Suter, C.E. Krill III, A.R. Krause, Observations of unexpected grain boundary migration in $SrTiO_3$, Scripta Mater 222 (2023) 115055, https://doi.org/10.1016/j.scriptamat.2022.115055.
[11] Z. Xu, Y.-F. Shen, S.K. Naghibzadeh, X. Peng, V. Muralikrishnan, S. Maddali, D. Menasche, A.R. Krause, K. Dayal, R.M. Suter, G.S. Rohrer, Grain boundary migration in polycrystalline α-Fe, Acta Mater. 264 (2024) 119541, https://doi.org/10.1016/j.actamat.2023.119541.
[12] J. Zhang, W. Ludwig, Y.B. Zhang, H.H.B. Sorensen, D.J. Rowenhorst, A. Yamanaka, P.W. Voorhees, H.F. Poulsen, Grain boundary mobilities in polycrystals, Acta Mater. 191 (2020) 211–220, https://doi.org/10.1016/j.actamat.2020.03.044.
[13] G.B. Bizana, L.A. Barrales-Mora, Kinetics of grain boundary migration in nanosized Al polycrystals, Acta Mater. 206 (2023) 119261, https://doi.org/10.1016/j.actamat.2023.119261.
[14] M. Lyu, Z. Xu, G.S. Rohrer, E.A. Holm, Comparing molecular dynamics simulations of grain growth with experimental data, Scripta Mater 256 (2025) 116429, https://doi.org/10.1016/j.scriptamat.2024.116429.
[15] S.K. Naghibzadeh, Z. Xu, D. Kinderlehrer, R. Suter, K. Dayal, G.S. Rohrer, Impact of grain boundary energy anisotropy on grain growth, Phys. Rev. Mater. 8 (2024) 093403, https://doi.org/10.1103/PhysRevMaterials.8.093403.
[16] C.H. Qiu, D.J. Srolovitz, G.S. Rohrer, J. Han, M. Salvalaglio, Why grain growth is not curvature flow, Proc. Natl. Acad. Sci. u S. a 122 (2025) e2500707122, https://doi.org/10.1073/pnas.2500707122.
[17] K.H. Blixt, H. Hallberg, Grain boundary stiffness based on phase field crystal simulations, Mater. Lett. 318 (2022) 132178, https://doi.org/10.1016/j.matlet.2022.132178.
[18] K.H. Blixt, H. Hallberg, Evaluation of grain boundary energy, structure and stiffness from phase field crystal simulations, Model. Simul. Mater. Sci. Eng. 30 (2022) 014002, https://doi.org/10.1088/1361-651X/ac3ca1.
[19] S.M. Foiles, J.J. Hoyt, Computation of grain boundary stiffness and mobility from boundary fluctuations, Acta Mater. 54 (2006) 3351–3357, https://doi.org/10.1016/j.actamat.2006.03.037.
[20] Z.T. Trautt, M. Upmanyu, Direct two-dimensional calculations of grain boundary stiffness, Scripta Mater 52 (2005) 1175–1179, https://doi.org/10.1016/j.scriptamat.2004.12.033.
[21] M. Upmanyu, Grain boundary stiffness based on a dislocation model, Scripta Mater 56 (2007) 553–556, https://doi.org/10.1016/j.scriptamat.2006.09.035.
[22] J.E. Taylor, J.W. Cahn, Shape accommodation of a rotating embedded crystal via a new variational formulation, Interfaces Free Boundaries 9 (2007) 493–512, https://doi.org/10.4171/IFB/174.
[23] J.E. Taylor, J.W. Cahn, C.A. Handwerker, Overview No. 98 I—Geometric models of crystal growth, Acta Metall Mater 40 (1992) 1443–1474, https://doi.org/10.1016/0956-7151(92)90090-2.
[24] G.S. Rohrer. Grain Boundary Data Archive, http://mimp.materials.cmu.edu/~gr20/Grain_Boundary_Data_Archive/.
[25] A. Bhattacharya, Y.F. Shen, C.M. Hefferan, S.F. Li, J. Lind, R.M. Suter, G.S. Rohrer, Three-dimensional observations of grain volume changes during annealing of polycrystalline Ni, Acta Mater. 167 (2019) 40–50, https://doi.org/10.1016/j.actamat.2019.01.022.
[26] C.M. Hefferan, S.F. Li, J. Lind, U. Lienert, A.D. Rollett, P. Wynblatt, R.M. Suter, Statistics of high purity nickel microstructure from high energy X-ray diffraction microscopy, CMC-comput, Mat. Contin. 14 (2009) 209–219, https://doi.org/10.3970/cmc.2009.014.209.
[27] M.A. Groeber, M.A. Jackson, DREAM.3D: a digital representation environment for the analysis of microstructure in 3D, Integr. Mater. Manuf. I. 3 (2014) 56–72, https://doi.org/10.1186/2193-9772-3-5.
[28] D.A. Field, Laplacian smoothing and Delaunay triangulations, Comm. Appl. Numer. Methods 4 (1988) 709–712, https://doi.org/10.1002/cnm.1630040603.
[29] J. Goldfeather, V. Interrante, A novel cubic-order algorithm for approximating principal direction vectors, ACM Trans. Graph. 23 (2004) 45–63, https://doi.org/10.1145/966131.966134.
[30] G.S. Rohrer. 3D_dist_graph, https://github.com/gr20cmu/gbXstallography/tree/main/3D_dist_graph.
[31] C. Herring, The use of classical macroscopic concepts in surface energy problems, in: R. Gomer, C.S. Smith (Eds.), Structure and Properties of Solid Surfaces; Proceedings of a Conference Arranged by the National Research Council and Held in September 1952, in Lake Geneva, Wisconsin, USA, University of Chicago Press, Chicago, 1953, pp. 5–81.
[32] K. Glowinski, A. Morawiec, A toolbox for geometric grain boundary characterization, in: 1st International Conference on 3D Materials Science, 2012, pp. 119–124, https://doi.org/10.1002/9781118686768.ch18.
[33] D.L. Olmsted, E.A. Holm, S.M. Foiles, Survey of computed grain boundary properties in face-centered cubic metals-II: grain boundary mobility, Acta Mater. 57 (2009) 3704–3713, https://doi.org/10.1016/j.actamat.2009.04.015.
[34] S.L. Thomas, K.T. Chen, J. Han, P.K. Purohit, D.J. Srolovitz, Reconciling grain growth and shear-coupled grain boundary migration, Nat. Comm. 8 (2017) 1764, https://doi.org/10.1038/s41467-017-01889-3.
[35] M.J. Xu, K.T. Chen, F. Cao, L. Velasco, T.M. Kaufman, F. Ye, H. Hahn, J. Han, D. J. Srolovitz, X.Q. Pan, Disconnection-mediated Twin/Twin-junction migration in FCC metals, Acta Mater. 240 (2022) 118339, https://doi.org/10.1016/j.actamat.2022.118339.
[36] Z. Xu, C.M. Hefferan, S.F. Li, J. Lind, R.M. Suter, F. Abdeljawad, G.S. Rohrer, Energy dissipation by grain boundary replacement during grain growth, Scripta Mater 230 (2023) 115405, https://doi.org/10.1016/j.scriptamat.2023.115405.

Supplemental Information: Can the grain boundary stiffness driving force explain observed grain boundary migration rates in polycrystals?

Zipeng Xu[1], Fadi Abdeljawad[2], and Gregory S. Rohrer[1]

[1]Department of Materials Science and Engineering, Carnegie Mellon University, Pittsburgh, PA 15213

[2]Department of Materials Science and Engineering, Lehigh University, Bethlehem, PA 18015

S.1. Grain boundary mesh treatment and velocity determination

Determining curvatures from discrete voxel data requires some level of processing and interpretation; we used Dream.3D's Laplacian smoothing. In the filter, we used 100 iterations and λ values of 0.25 (surface), 0.20 (triple lines), and 0.15 (quadruple points). These settings were chosen to balance de-voxelization against geometric bias: (i) they reduce staircase artifacts while (ii) keeping boundary shrinkage and node drift bounded. Lower λ/iterations under-smooth and leave voxel steps; higher values round triple junctions and distort dihedral angles. The parameters are also consistent with studies of the sensitivity of the curvature to smoothing parameters [1]. Curvatures determined from simulations of grains [1] indicate that objects with a radius greater than or equal to nine voxels deviate from the ideal value by less than 10 %. The mean grain radius in this sample was about nine voxels.

The velocity measurement is based on counting the number of voxels exchanged between grains and not on determining the interface position [2, 3]. Although the voxels exchanged can be counted with no error, some uncertainty stems from the segmentation of the data and results from voxels with possibly misassigned orientations. For different boundaries, the number of voxels exchanged ranged from zero to more than 300 and the mean value is 141; the distribution of exchanged voxels, illustrated in Fig. S1, peaks at zero, suggesting good alignment of the data.

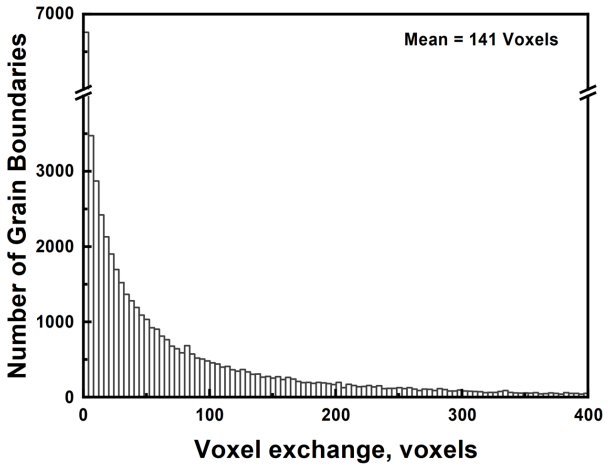

Figure S1. Distribution of the number of voxels exchanged across each grain boundary.

S2. Determining the interface stiffness tensor using experimental data

For each triangular mesh element of a boundary that has misorientation with a known energy function, $\gamma(\hat{\mathbf{n}})$, the stiffness tensor of the local boundary can be determined in the following way:

1. The interface normal vector $\hat{\mathbf{n}}$, defined in the sample reference frame, is first transfomed into the crystal reference frame $\hat{\mathbf{n}}_{\mathbf{crystal}}$ using the 3×3 orientation matrix $\mathbf{g_1}$ of crystal 1:

$$\hat{\mathbf{n}}_{\mathbf{crystal}} = \mathbf{g_1}\hat{\mathbf{n}}, \tag{S.1}$$

2. The reference frames of stiffness functions defined in references [4, 5] vary depending on the grain boundary misorientation. For example, grain boundaries with a 60°/[111] misorientation use the following crystal reference frame: $[11\bar{2}] \rightarrow$ X axis; $[\bar{1}10] \rightarrow$ Y axis; $[111] \rightarrow$ Z axis. The relationship between these reference frames is expressed by the 3 × 3 orientation matrix $\mathbf{T_m}$. This is used to transform $\mathbf{n}_{\mathbf{crystal}}$ from the crystal reference frame into the stiffness-function-defined reference frame $\hat{\mathbf{n}}_{\mathbf{tm}}$:

$$\hat{\mathbf{n}}_{\mathbf{tm}} = \mathbf{T_m}\hat{\mathbf{n}}_{\mathbf{crystal}}, \tag{S.2}$$

3. Finally, the interface normal vector $\hat{\mathbf{n}}_{\mathbf{tm}}$ is converted into spherical coordinates (θ, ϕ).

The interface stiffness tensor $\boldsymbol{\Gamma}(\theta, \phi)$ can then be determined by [4]:

$$\boldsymbol{\Gamma}(\boldsymbol{\theta}, \boldsymbol{\phi}) = \begin{bmatrix} \boldsymbol{\gamma_{\theta\theta}} & \dfrac{\mathbf{1}}{\mathbf{sin\theta}}\boldsymbol{\gamma_{\theta\phi}} - \dfrac{\mathbf{cos\theta}}{\mathbf{sin^2\,\theta}}\boldsymbol{\gamma_{\phi}} \\ \dfrac{\mathbf{1}}{\mathbf{sin\theta}}\boldsymbol{\gamma_{\theta\phi}} - \dfrac{\mathbf{cos\theta}}{\mathbf{sin^2\,\theta}}\boldsymbol{\gamma_{\phi}} & \boldsymbol{\gamma} + \dfrac{\mathbf{1}}{\mathbf{sin^2\,\theta}}\boldsymbol{\gamma_{\theta\theta}} + \dfrac{\mathbf{cos\theta}}{\mathbf{sin\theta}}\boldsymbol{\gamma_{\theta}} \end{bmatrix}, \tag{S.3}$$

S3. Determining the curvature tensor in the stiffness-function-defined reference frame

To calculate the stiffness driving force defined in Eq. 1, the stiffness tensor and the curvature tensor must be expressed in the same reference frame and in the same coordinates. The parameters and reference frame of the stiffness tensor has been described in section S2. The curvature tensor is originally computed in the sample reference frame by Dream 3D [6]. Therefore, the curvature tensor must be transformed from the sample frame to the spherical coordinate system used by the stiffness tensor. This is executed using the following steps.

1. First, the principal curvature directions $\mathbf{K_1}$, $\mathbf{K_2}$ are rotated from the sample reference frame into the stiffness-defined reference frame:

$$\mathbf{K_{tm_i}} = \mathbf{T_m} \cdot \mathbf{g_1} \cdot \mathbf{K_i} \ \ (\mathbf{i = 1, 2}) \tag{S.1}$$

Here, g_1 is the 3×3 orientation matrix of crystal 1 and $\mathbf{T_m}$ is the transformation matrix to the stiffness reference frame. Note that the local interface normal $\hat{\mathbf{n}}$ is always orthogonal to both principal directions.

2. Using the principal curvature directions in the correct reference frame and the corresponding principal curvatures κ_1 and κ_2, the curvature tensor, κ_{tm}, can be constructed:

$$\boldsymbol{\kappa_{tm}} = \sum_{\mathbf{i}} \boldsymbol{\kappa_i} \cdot \mathbf{K_{tm_i}} \otimes \mathbf{K_{tm_i}} \ (\mathbf{i = 1, 2}) \tag{S.5}$$

where $\otimes$ denotes the outer product.

3. The local basis vectors are defined in the following way. The unit surface normal $\hat{\mathbf{n}}(\theta, \phi)$ is defined as:

$$\hat{\mathbf{n}}(\boldsymbol{\theta}, \boldsymbol{\phi}) = \begin{bmatrix} \sin\boldsymbol{\theta}\cos\boldsymbol{\phi} \\ \sin\boldsymbol{\theta}\sin\boldsymbol{\phi} \\ \cos\boldsymbol{\phi} \end{bmatrix}, \tag{S.6}$$

The local in-plane basis vector $\hat{e}_\theta$, $\hat{e}_\phi$ – representing gradients in the azimuthal and polar directions respectively – are given by:

$$\hat{\mathbf{e}}_{\boldsymbol{\theta}} = \frac{\partial \hat{\mathbf{n}}}{\partial \boldsymbol{\theta}} = \begin{bmatrix} \cos\boldsymbol{\theta}\cos\boldsymbol{\phi} \\ \cos\boldsymbol{\theta}\sin\boldsymbol{\phi} \\ -\sin\boldsymbol{\theta} \end{bmatrix}, \hat{\mathbf{e}}_{\boldsymbol{\phi}} = \frac{1}{\sin\boldsymbol{\theta}} \frac{\partial \hat{\mathbf{n}}}{\partial \boldsymbol{\phi}} = \begin{bmatrix} -\sin\boldsymbol{\phi} \\ \cos\boldsymbol{\phi} \\ 0 \end{bmatrix} \tag{S.7}$$

4. The final curvature tensor in spherical coordinates $\kappa^{(\theta,\phi)}$ is obtained by projecting κ_{tm} onto the local spherical basis:

$$\boldsymbol{\kappa}_{\mathbf{i,j}}^{(\boldsymbol{\theta},\boldsymbol{\phi})} = \hat{\mathbf{e}}_{\mathbf{i}}^{\mathbf{T}} \cdot \boldsymbol{\kappa}_{\mathbf{tm}} \cdot \hat{\mathbf{e}}_{\mathbf{j}} \;\; (\mathbf{i}, \mathbf{j} \in \{\boldsymbol{\theta}, \boldsymbol{\phi}\}) = \mathbf{K} \tag{S.8}$$

This projection yields a symmetric second-rank tensor, referred to as K in Eq. 1. It was verified that the principal curvature values remain unchanged after the rotation, as the process only changes the basis. Once aligned, the interface driving force can be evaluated as the double dot product between the stiffness tensor $\boldsymbol{\Gamma}(\theta, \phi)$ and curvature tensor K.

S4. Supplemental Figures S2 to S7

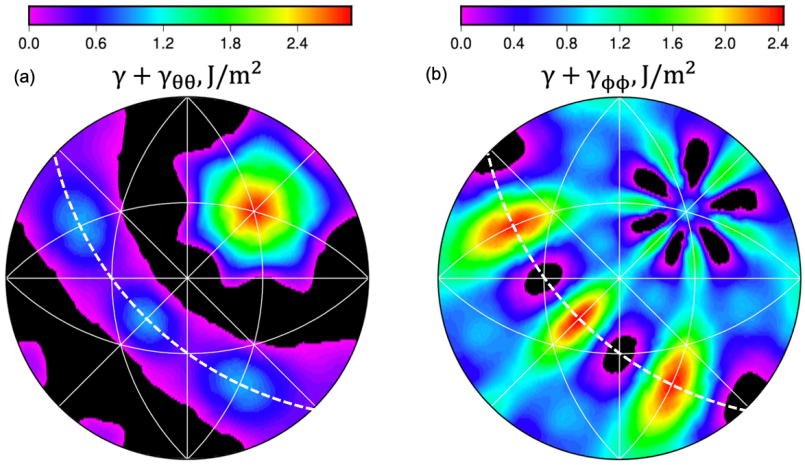

Figure S2. Stereographic projections along [001] showing principle stiffness distributions for 2,139 60°/[111] grain boundaries comprised of 1,085,836 individual mesh triangles. (a) and (b) Principal stiffness distributions $\gamma + \gamma_{\theta\theta}$ and $\gamma + \gamma_{\phi\phi}$, respectively, with black regions denoting negative values (51% of the area).

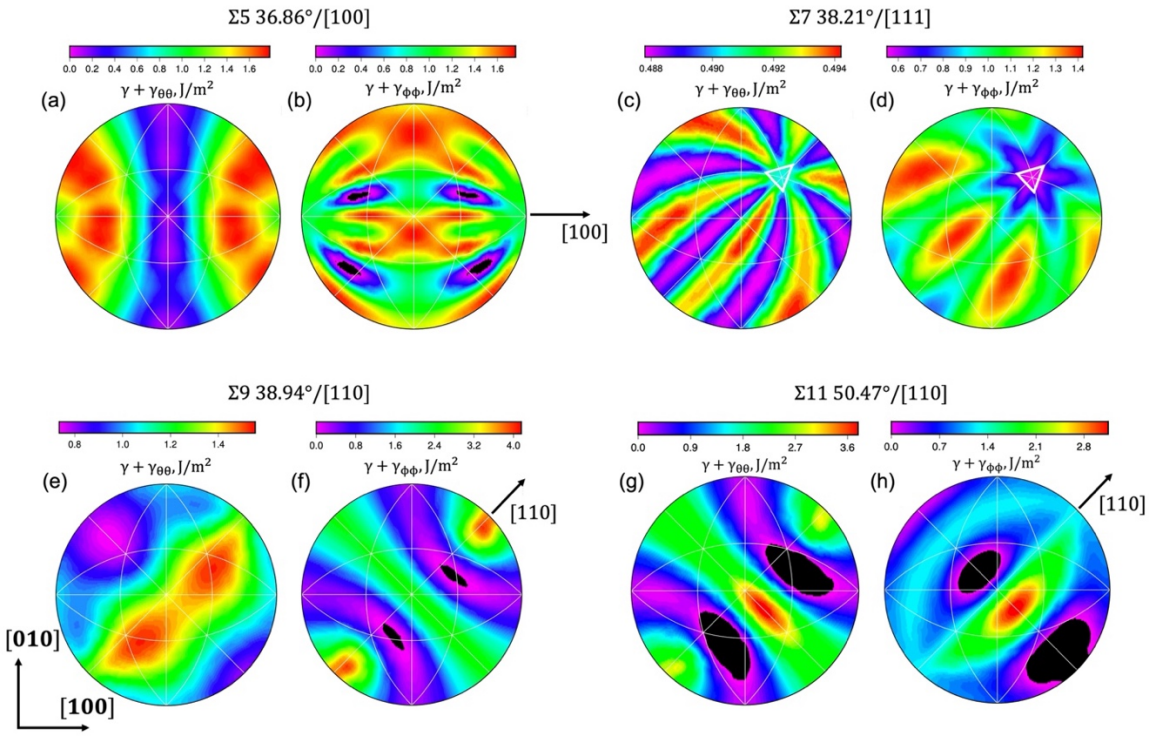

Figure S3. Principal stiffness distributions $\gamma + \gamma_{\theta\theta}$ and $\gamma + \gamma_{\phi\phi}$ for boundaries with 37°/[100] (Σ5), 38°/[111] (Σ7), 39°/[110] (Σ9), and 50°/[110] (Σ11) misorientations, with black regions denoting negative values which make up (a) 5 % , (b) 0 %, (c) 3 %, and (d) 24 % of the area. (a) - (b) Principal stiffness distributions of $\Sigma 5$ boundaries, the orientation of the [100] misorientation axis is shown by the arrow; (c) - (d) Principal stiffness distributions of $\Sigma 7$ boundaries, the direction of the misorientation axis [111] is denoted by the white triangle; (e) - (f) Principal stiffness distributions of $\Sigma 9$ boundaries, the orientation of the [110] misorientation axis is shown by the arrow; (g) - (h) Principal stiffness distributions of $\Sigma 11$ boundaries, the orientation of the [110] misorientation axis is shown by the arrow.

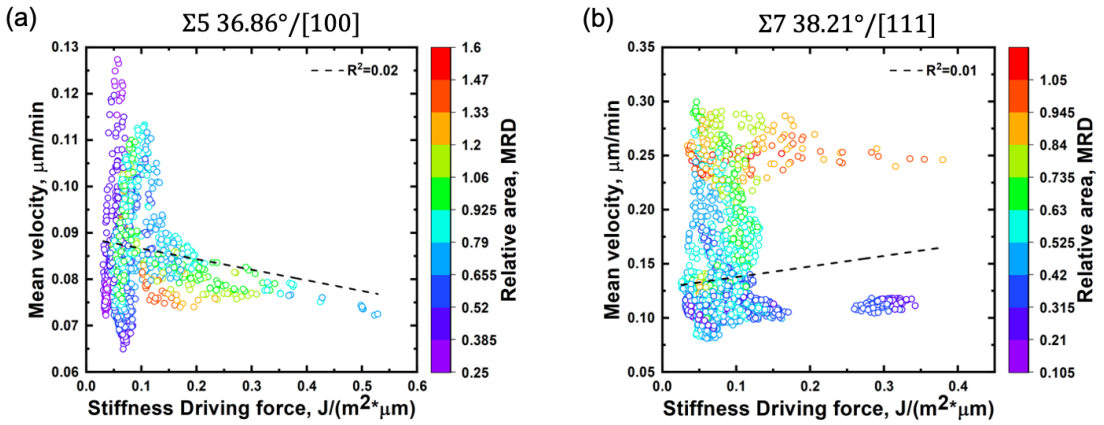

Figure S4. Correlation between grain boundary velocity and the stiffness driving force for 36.9°/[100] and 38.2°/[111] grain boundaries. Each data point represents a distinct grain boundary plane normal orientation and is colored by the corresponding relative area fraction within the total grain boundary population (MRD scale). (a) 215,653 triangles from 354 $\Sigma 5$ 36.9°/[100] boundaries; (b) 96,529 triangles from 453 $\Sigma 7$ 38.2°/[111] boundaries Correlation coefficients (R^2) and fitted trend lines are indicated for each boundary type.

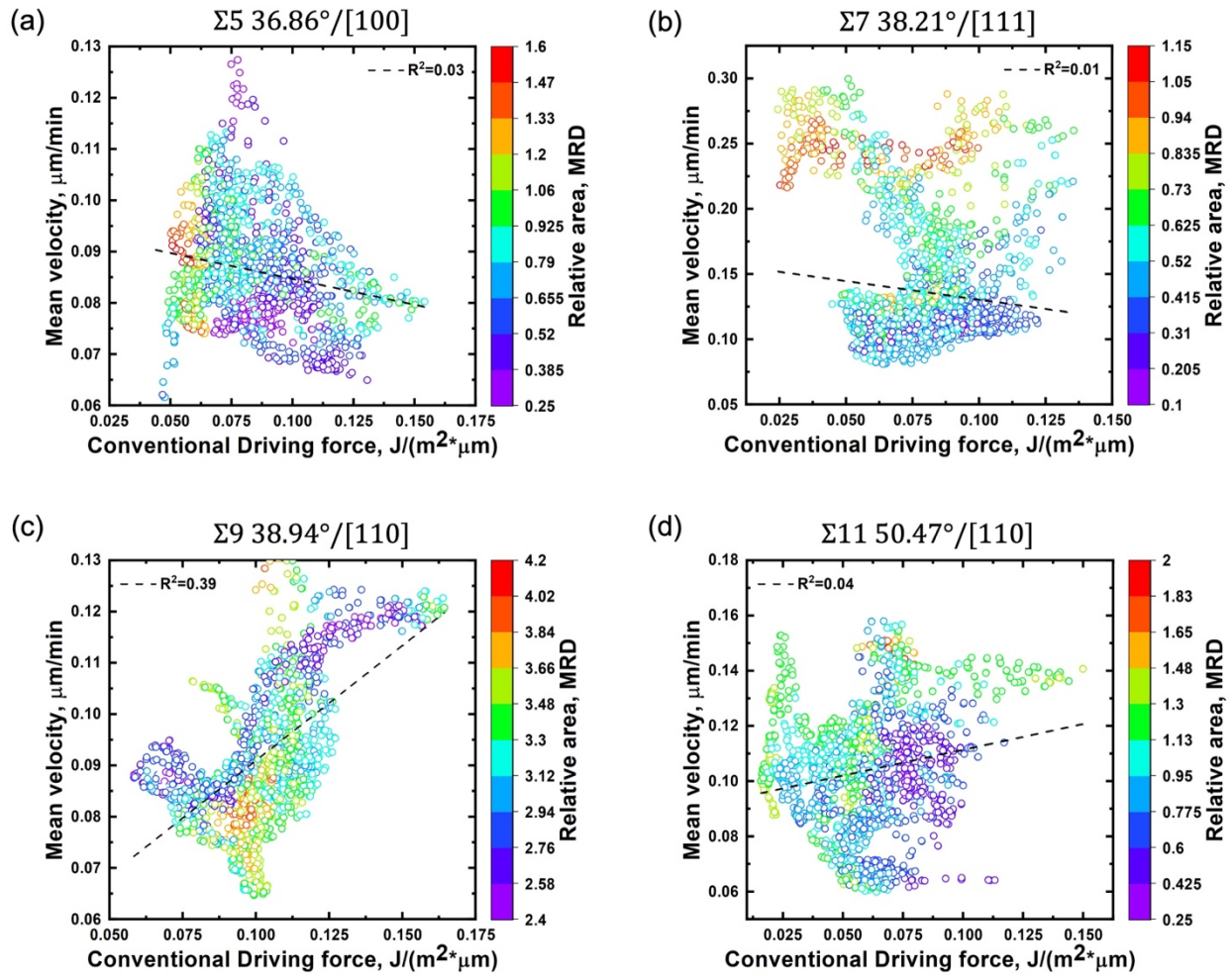

Figure S5. Correlation between grain boundary velocity and conventional driving force for various CSL boundaries. Each data point represents a distinct grain boundary plane normal orientation and is colored by the corresponding relative area fraction within the total grain boundary population (MRD scale). (a) 215,653 triangles from 354 $\Sigma 5$ 36.86°/[100] boundaries; (b) 96,529 triangles from 453 $\Sigma 7$ 38.21°/[111] boundaries; (c) 837,206 triangles from 3804 $\Sigma 9$ boundaries; (d) 215,653 triangles from 751 $\Sigma 11$ boundaries. Correlation coefficients (R^2) and fitted trend lines are indicated for each boundary type.

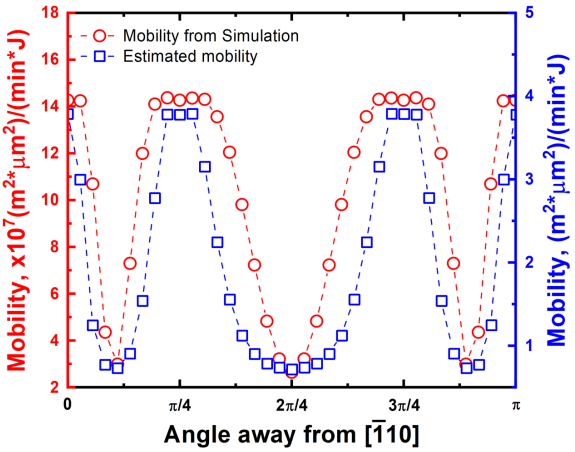

Figure S6. Correlation between the effective grain boundary mobility estimated by dividing the experimental velocity by stiffness driving force and the mobility from calculation [4, 7] as a function of angular deviation from $(\bar{1}10)$ for tilt boundaries with a 60°/[111] misorientation. Data points represent averaged values computed from all mesh triangles with plane normal deviating less than 7° from the target orientation vector.

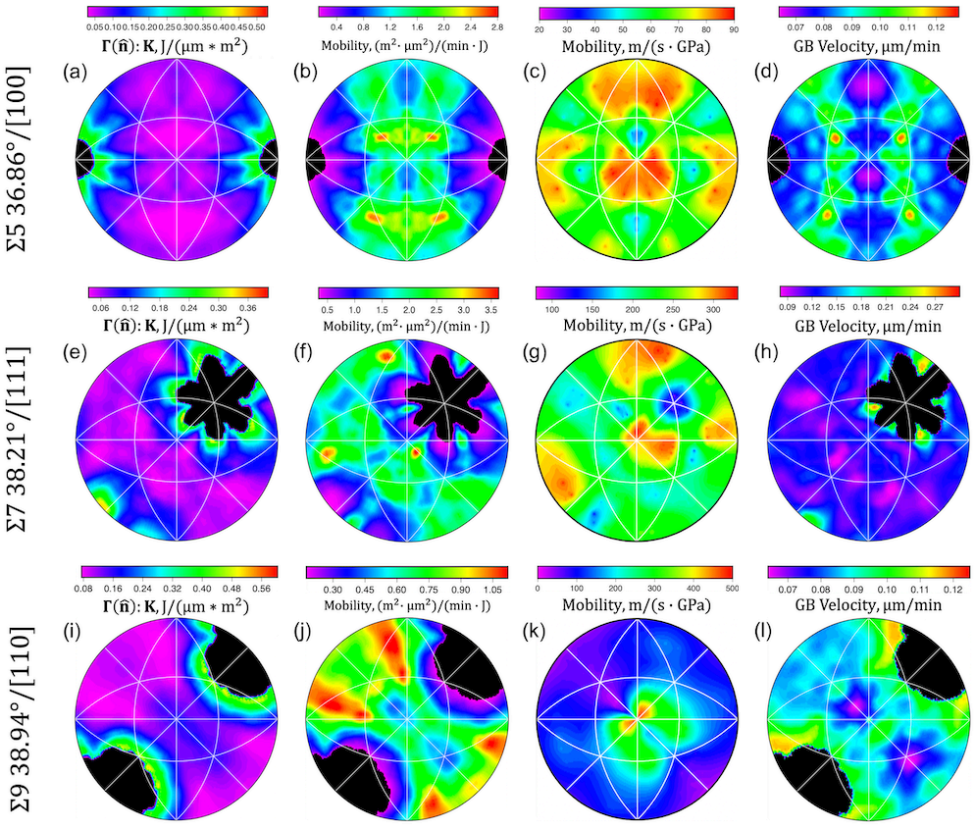

Figure S7. Comparison of the stiffness driving force, effective mobility computed by dividing the measured velocity by the stiffness driving force, the computed mobility [7], and the measured velocity for the 37°/[100] (Σ5), 38°/[111] (Σ 7), and 39°/[110] (Σ9) grain boundaries.

S5. Shortest distance method for tracking meshed triangles in two states

The function tracks the velocity of grain boundary triangles by matching each triangle in the initial state to its nearest neighbor in the final state. The method assumes that all meshed triangles that belong to the initial state can be matched to the final state. It identifies the closest centroid in the final state for each triangle in the initial state using a KD-tree nearest-neighbor search. The resulting displacement vectors between matched centroids provides a measure of motion, and projecting these displacements along the computed normals gives the normal displacements. The displacements are plotted versus driving force in Fig. S8.

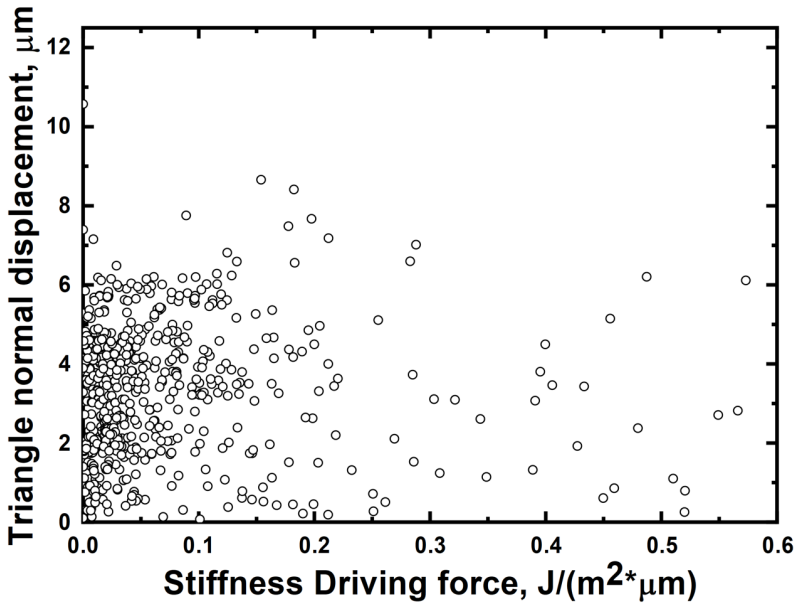

Figure S8. Correlation between stiffness driving force and corresponding triangle normal displacement for the boundary visualized in Fig. 5.

References

[1] X.T. Zhong, D.J. Rowenhorst, H. Beladi, G.S. Rohrer. The five-parameter grain boundary curvature distribution in an austenitic and ferritic steel, Acta Mater. 123 (2017) 136-145, http://dx.doi.org/10.1016/j.actamat.2016.10.030.

[2] A. Bhattacharya, Y.F. Shen, C.M. Hefferan, S.F. Li, J. Lind, R.M. Suter, C.E. Krill, G.S. Rohrer. Grain boundary velocity and curvature are not correlated in Ni polycrystals, Science 374 (2021) 189-193, http://dx.doi.org/10.1126/science.abj3210.

[3] Z. Xu, Y.-F. Shen, S.K. Naghibzadeh, X. Peng, V. Muralikrishnan, S. Maddali, D. Menasche, A.R. Krause, K. Dayal, R.M. Suter, G.S. Rohrer. Grain boundary migration in polycrystalline α-Fe, Acta Mater. 264 (2024) 119541, http://dx.doi.org/https://doi.org/10.1016/j.actamat.2023.119541.

[4] F. Abdeljawad, S.M. Foiles, A.P. Moore, A.R. Hinkle, C.M. Barr, N.M. Heckman, K. Hattar, B.L. Boyce. The role of the interface stiffness tensor on grain boundary dynamics, Acta Mater. 158 (2018) 440-453, http://dx.doi.org/10.1016/j.actamat.2018.06.025.
[5] R.D. Moore, T. Beecroft, G.S. Rohrer, C.M. Barr, E.R. Homer, K. Hattar, B.L. Boyce, F. Abdeljawad. The grain boundary stiffness and its impact on equilibrium shapes and boundary migration: Analysis of the Sigma 5, 7, 9, and 11 boundaries in Ni, Acta Mater. 218 (2021) 117220, http://dx.doi.org/10.1016/j.actamat.2021.117220.
[6] M.A. Groeber, M.A. Jackson. DREAM.3D: A Digital Representation Environment for the Analysis of Microstructure in 3D, Integr. Mater. Manuf. I. 3 (2014) 56-72, http://dx.doi.org/10.1186/2193-9772-3-5.
[7] D.L. Olmsted, E.A. Holm, S.M. Foiles. Survey of computed grain boundary properties in face-centered cubic metals-II: Grain boundary mobility, Acta Mater. 57 (2009) 3704-3713, http://dx.doi.org/10.1016/j.actamat.2009.04.015.